Prospects for the diagnosis of breast cancer by noninvasive probing of calcifications using transmission Raman spectroscopy

Pavel Matousek
Council for the Central Laboratory of the Research Councils
Rutherford Appleton Laboratory
Central Laser Facility
Oxfordshire OX11 0QX, United Kingdom
E-mail: p.matousek@rl.ac.uk

Nicholas Stone
Gloucestershire Royal Hospital
Biophotonics Research Group
Great Western Road
Gloucester GL1 3NN, United Kingdom

Abstract. Breast calcifications can be found in both benign and malignant lesions, and the composition of these calcifications can indicate the possible disease state. As current practices such as mammography and histopathology examine the morphology of the specimen, they cannot reliably distinguish between the two types of calcification, which frequently are the only mammographic features that indicate the presence of a cancerous lesion. Raman spectroscopy is an optical technique capable of obtaining biochemical information of a sample *in situ*. We demonstrate for the first time the noninvasive recovery of Raman spectra of calcified materials buried within a chicken breast tissue slab 16 mm thick, achieved using transmission Raman spectroscopy. The spectra of both calcium hydroxyapatite (HAP) and calcium oxalate monohydrate (COM) are obtained and chemically identified. The experimental geometry and gross insensitivity of the Raman signal to the depth of the calcified lesion makes the concept potentially well suited for probing human female breasts, in conjunction with existing mammography or ultrasound, to provide complementary data in the early diagnosis of breast cancer. [DOI: 10.1117/1.2718934]

Keywords: spatially offset Raman spectroscopy; cancer; transmission; Raman; noninvasive; turbid; breast; calcifications.

Paper 06262R received Sep. 20, 2006; revised manuscript received Nov. 17, 2006; accepted for publication Dec. 26, 2006; published online Apr. 3, 2007.

1 Introduction

1.1 *Calcifications in Breast Cancer*

Calcifications are found in many different biological tissues, forming both as natural products (e.g., in bones and teeth) and in soft tissues as a result of disease. Natural calcifications are present as a mineralization product in bone, and consist of the specific mineral hydroxyapatite. Pathological calcifications are associated with many medical conditions such as diabetes, breast cancer, and crystals-associated osteoarthritis. The deposition of calcium crystals on cells induces detrimental cellular effects and speeds up the progression of the associated diseases.[1] Several studies have been carried out using different techniques to examine calcifications forming inside breast tissue, but as yet their formation mechanisms and biological impact on the tissue remain unclear. The presence of calcifications on mammography is a feature of particular diagnostic significance, as sometimes this may be the only marker of a malignant breast lesion. Mammography can detect small masses, areas of distortion, ill-defined densities, and microcalcifications not detectable by physical examination. However, as this relies only on the morphology of the specimen, it has no definitive criteria for classifying benign and malignant calcifications. It has, in fact, been found that 70 to 90% of mammographically detected lesions are found to be benign upon needle biopsy.[2]

Microcalcifications can be divided into two types; type 1, which consist of calcium oxalate dihydrate (COD), and type 2 deposits, which are composed of calcium phosphates, mainly calcium hydroxyapatite (HAP). At present, there is no reliable way to distinguish between these two types of calcification by mammography, but the type is thought to correlate with disease.[3] Calcium oxalate crystals are mainly found in benign ductal cysts and rarely found in carcinoma,[4] whereas calcium hydroxyapatite deposits are found both in carcinoma and in benign breast tissue.[3] Furthermore, it has been shown that type 2 calcifications found in benign ducts appear spectroscopically distinct from type 2 calcifications found in malignant lesions. The benign hydroxyapatite calcifications have been shown to contain larger concentrations of calcium carbonate.[3]

As there are differences in chemistry between these two types of calcification, significant insight may be gained by using vibrational spectroscopy to probe their biochemical composition. If such a technique could be utilized *in vivo*, this might enable a more simplistic decision for diagnosing breast lesions and potentially reduce the patient trauma, time delay, and high medical costs associated with the biopsy of benign

Address all correspondence to Pavel Matousek, Central Laser Facility, Rutherford Appleton Laboratory, Chilton - Didcot, Oxfordshire 0X11 0QX, United Kingdom; Tel: +44(0)1235 445377; Fax: +44(0)1235 445693; E-mail: p.matousek@rl.ac.uk

1083-3668/2007/12(2)/024008/8/$25.00 © 2007 SPIE

lesions, as the detection of COD compound would signify the presence of benign cancer.

1.2 *Raman Spectroscopy*

Raman spectroscopy is a sensitive, chemical specific analytical technique capable of providing highly detailed biochemical information on tissue samples *in vivo*. Previous experiments have demonstrated the ability of Raman spectroscopy to distinguish between normal and malignant tissues[5–10] and in different grades of abnormal breast tissue.[3,11] It has recently been shown that Raman spectroscopy is capable of distinguishing the two types of calcification in excised breast tissue with a high degree of accuracy.[3] However, until recently, it could be applied to probing tissue in depths of only several hundred micrometers, due to the diffusely scattering nature of tissue preventing the formation of sharp optical images required by confocal Raman microscopy. This study investigates the potential of diffuse components of light to render Raman spectra from beneath the tissue surface of several millimeters, which is needed for the detection of microcalcifications inside breast tissue.

Raman spectroscopy, when deployed in its conventional backscattering geometry to deep layer probing of turbid media, has an exceptionally strong bias to the surface layers of a sample, as we have shown earlier.[12] This applies to both Raman and fluorescence signals and is highly undesirable in noninvasive deep tissue Raman spectroscopy. Consequently, the Raman contributions from the inner sample regions are often overwhelmed by those originating from the surface layers (e.g., melanin in surface layers of skin), leaving information relating to the internal composition of the sample masked. Here we demonstrate how the adoption of transmission geometry[12,13] with Raman spectroscopy for nonabsorbing or weakly absorbing diffusely scattering samples can practically eliminate this bias, and enable detailed spectroscopic information relating to the interior of the sample to be obtained. In this approach, the laser beam is incident on one side of the probed object, and the Raman light is collected from the opposite side [see Fig. 1(a)]. This geometry is compatible with breast mounts used in conventional mammography, where the breast is inserted between two plates that are slightly compressed against each other, diminishing its thickness to several centimeters.

The properties of generating Raman light and its behavior in deep layers of turbid media such as living tissue are governed chiefly by the "random walk" made by the laser photons migrating through the sample and producing Raman photons that randomly migrate within the probed medium. The earliest experimental work aimed at probing deeply buried structures in turbid media include studies using confocal Raman microscopy and time-resolved Raman spectroscopy in media, such as suspensions of polystyrene spheres[14] and milk,[15] that built on the extensive work of others on elastically scattered light.[16–18] Recent studies have revealed that, in turbid media, the Raman component decays more slowly than its elastically scattered counterpart, a process which conveniently offsets the inherent weakness of Raman spectroscopy in deep layer spectroscopy.[19] The reason for this is that the Raman component, initially present at zero intensity, is, on its pathway, constantly generated from the elastic component of light, offsetting its decay due to scattering, absorption, and loss on the air-to-sample interface. This is in contrast to the elastic component of light (laser photons), which does not experience any such rejuvenation and only decays monotonously away. The concerned strand of research stimulated the development of two principal noninvasive Raman methods: the temporal and spatial. The temporal approach relies on the impulsive excitation of the sample and picosecond time-resolved detection of the Raman signal using an optical Kerr gate.[19–25] The spatial approach is based on the collection of Raman signals from spatially offset regions away from the point of illumination on the sample surface—spatially offset Raman spectroscopy (SORS).[26–32] The SORS technique, in particular, shows promise for the probing of living tissue, as it is compatible with safer continuous-wave laser beams.

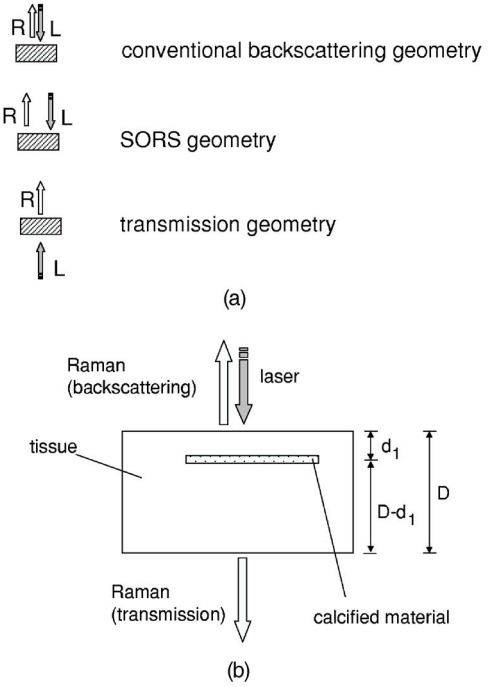

Fig. 1 (a) Illustration of the conventional Raman backscattering, SORS, and Raman transmission geometries. R is Raman light and L is the laser beam. (b) Experimental sample geometry with depiction of the backscattering and transmission Raman geometries along with the definition of parameters.

Our subsequent research has revealed useful properties of transmission Raman geometry when used with diffusely scattering media [see Fig. 1(a)]. Namely, its large insensitivity to depth, from which a signal is collected for a given thickness of the probed medium and the suppression of interference from Raman and fluorescence signals emanating from surface layers of a sample, properties that were shown to be ideally suited for bulk probing of pharmaceutical tablets[12] and colored pharmaceutical capsules or coated tablets.[33] In applications to human tissue, all these properties can be highly beneficial, too. The insensitivity to interference from Raman and fluorescence signals from surface layers enables the suppression of melanin-induced fluorescence from skin, and the depth insensitivity permits the monitoring of the presence of lesions irrespective of their depth, e.g., whether in the middle or at

the opposite side of the sample, in all cases yielding a similar level of the Raman signal with respect to the surrounding tissue.

This property can be qualitatively understood from the diagram shown in Fig. 1(b). In backscattering geometry, probe photons first have to reach the probed object (e.g., a lesion) buried in depth d_1. Upon Raman down conversion, the Raman photon then has to propagate the same distance d_1 (in both the cases in random walk fashion) to emerge on the surface. Therefore, the overall propagation distance is $d_{\text{total}}=2d_1$. It is intuitive that with the larger depths d_1, the overall propagation distance is going to be larger and consequently the weaker Raman signals would be expected. It should be remembered that the propagation distance d_{total} is propagated in random-walk-like fashion, and consequently a large dilution of signal is expected with the increase of the depth the photons have to traverse. In sharp contrast, in transmission geometry, the probe photons again first have to reach the target and traverse distance d_1 as in previous cases. However, the generated Raman photons then have to propagate to the other surface to be detected, i.e., they have to traverse distance $D-d_1$, where D is the overall thickness of the probed medium. The overall propagation distance in this case is therefore $d_{\text{total}}=d_1+D-d_1=D$, i.e., it is independent of the target depth d_1. Consequently, it is quite natural that the overall Raman signal intensity in transmission geometry should be largely insensitive to the depth of the probed target lesion. Although this picture is oversimplified, neglecting the effects stemming from the finite Raman collection aperture and beam size, it is valid in the first approximation, as we have shown using more detailed numerical simulations and experimentally on powders earlier.[12]

Unlike SORS, the transmission geometry concept in its basic form does not offer the ability to separate layers into individual components, but instead it yields, in a simple way, a high average-volume sample information superseding that obtainable with conventional approaches.[12] Consequently, it cannot yield the depth of the probed object. Nevertheless, this information is available from mammography or can be obtained using ultrasound or the previously mentioned SORS approach.

It should also be noted that transmission Raman can be viewed as being highly complementary to SORS, with SORS being beneficial in situations where mammography and transmission Raman cannot be used because of small breast size, or high density of breast tissue, which is known to significantly reduce the effectiveness of x-ray mammography for younger/premenopausal patients. Importantly, for this subset of individuals as well as for probing male breasts, SORS in its conventional backscattering mode may present the only means of locating and identifying suspected lesions. Although it should be pointed out that male breast cancer is a much rarer disease, with the occurrence of only 1 per 140 women cancers diagnosed.[34]

Recently, building on the prior developments, we have demonstrated experimentally the capability of the Raman Kerr gating approach to recover the Raman spectra of calcified material noninvasively behind 0.9 mm of chicken breast tissue.[35] This depth was subsequently increased to 8.7 mm utilizing the previously mentioned SORS method.[36] We report the reaching of a new milestone, the recovery of chemically specific information on calcified material through a 16-mm-thick slab of breast tissue using transmission Raman with all its benefits, representing thus the realization of clinically relevant depths for potential practical deployment *in vivo*. Chicken breast tissue was chosen to permit direct comparison with our earlier measurements, and also because it has remarkably similar Raman characteristics to human protein-rich tissue spectra at NIR wavelengths. However, we recognize that most human breasts are made up of fatty tissue with epithelial and stromal tissue within it, and consequently our spectra from the chicken breast tissue do not fully represent all of the signals expected from the human breast. This work should be considered to be a proof-of-concept study, and more advanced phantoms will be used in the next phase.

2 Numerical Model

A numerical model[27] has been used to elucidate the dependence of Raman signals in transmission geometry on the sample thickness. In the simulations, both the elastically (probe) and nonelastically scattered (Raman) photons are individually followed as they propagate through the medium in random-walk-like fashion in 3-D space.[16] A simplified assumption was made that in each step a photon propagates in a straight line over a distance t, and thereafter its direction is fully randomized at the next scattering event. This picture is somewhat simplistic from the standpoint of individual scattering events, which are often strongly biased toward the forward direction. However, we have shown that for large propagation distances such as those pertinent to the bulk analysis of breast tissue, as of interest here, this simplification is justifiable with appropriately chosen randomization length.[27] The propagation distance t, over which the photon direction is randomized, can be approximated as the transport length of the scattering medium (l_t),[15,16] which is defined as the average distance photons must travel within the sample before deviating significantly from their original direction of propagation. Our model considers the sample to be a homogeneous turbid medium with one air-medium interface located at the top surface $z=0$, where z is a Cartesian coordinate normal to the interface plane. The other sample-to-air interface exists at the opposite side of sample at the position $z=D$, where D is the sample thickness. The thickness of the medium D was varied from 2 to 34 mm in 2-mm steps.

The model assumes that all the probe photons are first placed at a depth equal to the transport length l_t and symmetrically distributed around the origin of the coordinate system x,y. The beam radius of the incident light is $r=3$ mm, and the beam has uniform intensity across it, i.e., we assume it has a flat, "top-hat" intensity profile, with all the photons having equal probability of being injected into the sample at any point within its cross section. The transmission Raman light is collected on the opposite side of the sample symmetrically around the projection axis of the top laser illumination area from an area of identical dimensions.

The numerical code was written in Mathematica 5.0 (Wolfram Research, Champaign, IL). One million photons were propagated simultaneously, each across an overall distance of 400 mm. On the propagation of this distance the calculations were stopped, thus approximating the presence of an absorption of OD $\sim$1 per 400 mm, as reported for bulk absorption

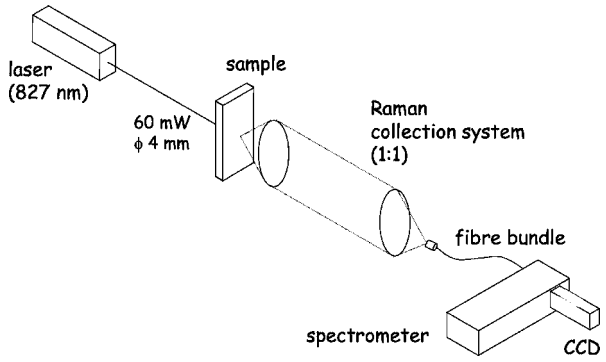

Fig. 2 Schematic of the experimental setup.

of human breast tissue at 800 nm.[37] The optical density accounting for the conversion of probe photons into Raman photons was set to 1 per 1000 mm. Although this value is higher than that of real conversion, it only affects the absolute number of Raman photons and not the spatial dependencies of concern to a significant degree in the studied regime, and was verified by varying this value up and down. The step size used was $t=1$ mm, approximating the bulk breast tissue scattering transport length at 800 nm.[37]

3 Experimental Section

The Raman spectra in this work were obtained using a modified SORS Raman apparatus developed for noninvasive spectroscopy of bones described earlier.[29] The probe beam was generated using a temperature stabilized diode laser for Raman spectroscopy and operating at 827 nm (Micro Laser Systems, Incorporated, Garden Grove, CA, L4 830S-115-TE). The laser power at the sample was about 60 mW at the sample, and the laser spot diameter before the sample was ~4 mm. The beam was spectrally purified by removing any residual amplified spontaneous emission components from its spectrum using two 830-nm bandpass filters (Semrock, Rochester, NY). These are slightly tilted to optimize their throughput for the 827-nm laser wavelength.

The Raman light was collected using a standard 50-mm-diam uncoated fused silica lens with a focal length of 60 mm. The scattered light was collimated and passed through a 50-mm-diam holographic notch filter (830 nm, Kaiser Optical Systems, Incorporated, Ann Arbor, MI) to suppress the elastically scattered component of light. The filter was also slightly tilted to optimize the suppression for the 827-nm elastic scatter. The second lens, identical to the first, was then used to image, with magnification 1:1, the sample interaction zone onto the front face of a fiber probe. The laser incident spot was positioned in such a way so that it coincided with the center of the SORS probe axis projected through the imaging system on the sample (see Fig. 2). Two more filters (25-mm-diam holographic notch filter, 830 nm, Kaiser Optical Systems, Incorporated, Ann Arbor, MI, and an edge filter, 830 nm, Semrock) were used just before the probe to suppress any residual elastically scattered light that passed through the first holographic filter. The fiber probe was comprised of seven fibers placed tightly packed at the center of the probe and 26 fibers distributed on a ring of 3 mm radius used in previous SORS measurements.[29] The fibers were made of silica with a core diameter of 200 μm, cladding diameter of 230 μm, and numerical aperture of 0.37. Sleeves were stripped on both ends for tighter packing of the fibers. The bundle was custom made by C Technologies, Incorporated, Bridgewater, NJ. The Raman light was propagated through the fiber systems of length ~1 m to the linear fiber end oriented vertically, and placed in the input image plane of a Kaiser Optical Technologies Holospec f=1.4 NIR spectrograph with its slit removed. In this orientation, the fibers themselves acted as the input slit of the spectrograph. The Raman spectra were collected using a NIR back-illuminated deep-depletion TE-cooled charge-coupled device (CCD) camera (Andor Technology, Belfast, Northern Ireland, DU420A-BR-DD, 1024×256 pixels) by binning the signal from both sets of fibers into a single spectrum (full vertical chip binning). The cosmic ray removal feature within the data acquisition software was not active. The Raman spectra are not corrected for the variation of detection system sensitivity across the observed spectral range. The acquisition time was 100 s for each spectrum. Following background subtraction, cosmic rays were removed from spectra and the spectra were then smoothed in Grams/AI software (Thermo Galactic, Woburn, MA) using the Savitzky-Golay method with a third-order polynomial function fitted across 11 points.

Polycrystalline standards were purchased (Clarkson Chromatography Products Incorporated, South Williamsport, PA) of "pure" calcium hydroxyapatite (HAP), calcium oxalate monohydrate (COM), and a 3.5% carbonate substituted hydroxyapatite (COHAP). The powders were placed into 2-mm-thick vials with 300-μm UV-grade quartz windows. Calcium oxalate dihydrate (COD) is difficult to manufacture due to its inherent thermodynamic instability. In this study, we used COM as a substance with similar properties to COD, but available for purchase (Sigma-Aldrich, St. Louis, MO).

Chicken breast and skin tissue were used in the model due to their homogenous nature. Normal fresh chicken breast was obtained and cut to the desired thickness. The samples were stored in a refrigerator and warmed to room temperature before use.

4 Results and Discussion

Figure 3(a) illustrates the dependence of transmission Raman signal of the bulk breast tissue on the thickness of the breast sample obtained using numerical simulations. The Raman signal initially rises, a phenomenon expected, as at very small thicknesses massive photon loss occurs at the sample-to-air interfaces, preventing appreciable buildup of Raman signal from laser photons. Ultimately, the Raman signal starts to diminish due to sideways photon diffusion, which overcomes the increase of Raman photon signals due to the longer pathways available. With larger thicknesses, photons gradually drift sideways, missing progressively more of the collection aperture. In addition, photon absorption comes to play a more prominent role.

Figure 3(b) illustrates the qualitative dependence of the transmission Raman signal of calcifications within breast tissue, assuming a fixed amount is contained in the tissue (e.g., around a cancer cluster) and its amount is independent of breast tissue overall thickness. The data were derived from

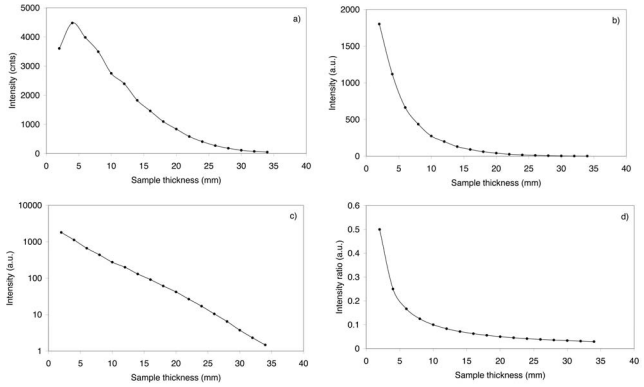

Fig. 3 (a) The dependence of the transmission Raman signal of bulk tissue on sample thickness. (b) The dependence of the transmission Raman signal of a layer of calcifications of fixed amount within a turbid medium on the overall medium thickness. (c) Logarithmic plot of data presented in (b). (d) The dependence of the intensity ratio of Raman calcification component to the bulk breast tissue Raman signals. The data are derived from Monte Carlo simulations.

Fig. 3(a) by dividing the intensity of the Raman signal by corresponding sample thickness. This procedure is justified by the fact that the signal in the transmission Raman signal is rather insensitive to the depth of a layer of constant thickness within the medium,[12] and consequently the signal strength of such a layer to that of the bulk medium can be approximated as the ratio of the thicknesses of this layer to the overall bulk medium thickness. This dependence is more representative of the real behavior, as calcifications typically cluster in and around cancerous lesions, and it is reasonable to expect that their amount would not vary largely with breast tissue thickness. Naturally, this dependence is steeper than that from the bulk medium alone, shown in Fig. 3(a), as the relative volume of calcification diminishes to the overall breast tissue volume with the increasing breast tissue thickness. The logarithmic plot of the same dependence is shown in Fig. 3(c). From this plot it is evident that the Raman signals of calcifications diminish more or less exponentially with breast tissue thickness, with the signal decreasing by an order of magnitude every 10 mm.

Another useful parameter is the dependence of the relative ratio of Raman signal intensities of the calcification to that of the overall breast tissue component. This is because the ability of recovering weaker Raman signals on top of a stronger Raman background depends critically on their relative intensity, as the stronger bulk signal effectively acts as a source of noise and can potentially swamp the weaker signal. This dependence is shown in Fig. 3(d). Conveniently, this parameter is a rather weak function of breast tissue thickness and implies that if Raman signals of calcifications can be recovered from depths of 10 to 20 mm, then recovery from 20- to 35-mm depths should still be within reach as, for example, this ratio is only weakly diminished by a factor of 2.1 when going from 16 to 34 mm.

Figure 4(a) illustrates the experimental result of probing calcified material contained within the quartz cell and placed in the middle (d_1=8 mm) of the tissue slab of an overall tissue thickness of D=16 mm, along with the spectra of tissue alone measured from the same slab in the absence of the cell and the Raman spectra of individual calcified compounds (COM and HAP) measured separately [see also Fig. 1(b) for the definition of parameters]. It is evident that the key markers of calcified compounds are clearly recognizable in the raw Raman spectra. These can be readily isolated from the background tissue signals by subtracting tissue only Raman spectra away from the individual spectra of tissue containing calcified material. The results of such subtraction, along with the Raman spectra of pure calcified compounds, are shown in Fig. 4(b). Identifiable Raman spectra of calcified materials are clearly visible after such subtraction. A measurement has also been performed on the same 16-mm slab in the presence of an additional layer of chicken skin added to one side of the slab, with the laser beam directly incident on the surface of the skin to include the scattering effects of the skin. The subtracted Raman spectra from this measurement are shown in Fig. 4(c). Again, even in this case, identifiable Raman spectra of calcified compounds are recovered.

Figure 5 shows the result of the same measurement as before on the 16-mm slab of chicken tissue but with a thin layer (100 to 300 μm) calcified material smeared in the middle of the slab used in place of the sample cell. Despite a substantially smaller amount of calcified material present, the identifiable Raman spectra of individual calcified compounds have also been recovered. The detectability of such a small amount of material is clearly possible because of much higher Raman scattering cross sections of the calcifications compared with that of surrounding tissue.

The attained depth of 16 mm is approaching the lower range of the clinically relevant depths required for the deployment of the technique in clinical environments for probing human breast tissue *in vivo*. Typical breast tissue thickness in mammography studies is around 5 cm with bottom ranges reported[38] starting from 1.9 cm. It should be noted that in mammography studies, the entire breast is flattened. In our measurements, a small cylindrical probe and cylindrical laser delivery head pressed against each other on opposite sides of the breast could be used instead. In such a configuration, the breast could be potentially compressed to a considerably smaller thickness at the probed area than that possible with parallel plates. The next part of our studies will aim at assessing the practical issues associated with the use of this technique for *in-vivo* probing in the clinical environment.

In terms of sensitivity to the clinically relevant concentration of calcifications, we estimate that this measurement sensitivity was around 2 orders of magnitude below the clinically relevant level. This assumption is based on a study of 1786 calcifications, with 2 to 193 calcifications per cluster, averaging 17 per cluster. The average size for malignant calcifications was 0.398 mm, and for benign calcifications 0.394 mm.[39] The average distance between calcifications within x-ray 2-D images in this study was 3.5 and 5 mm for benign and malignant calcifications, respectively. Thus calculating the ratio of average area of the calcifications to the area between them leads to 0.5% for malignant calcifications and 1.0% for benign calcifications in two dimensions for the x-ray image of the breast. Assuming the same cluster was within our 16-mm slab of tissue, the observable signal stemming from it would be 2 orders of magnitude lower than that detected in our measurement in Fig. 5, where we used an unin-

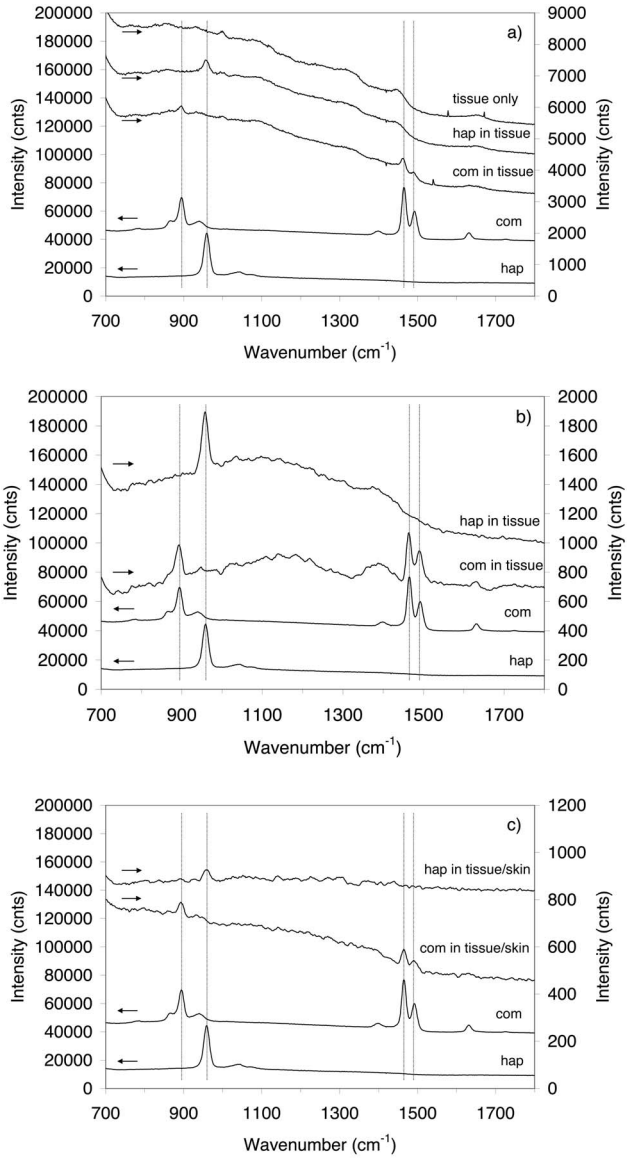

Fig. 4 (a) Raman spectra of calcified material (COM, HAP) contained within a 2-mm-thick cell placed in the middle of the tissue slab of an overall tissue thickness of 16 mm (HAP in tissue, COM in tissue), along with the spectra of tissue only measured from the same slab in the absence of the cell (tissue only), as well as Raman spectra of individual calcified materials measured separately (COM, HAP). (b) The Raman spectra of calcified materials, obtained by subtracting raw Raman spectra of tissue from those of tissue containing calcified material, along with the pure Raman spectra of individual calcified materials. (c) As in (b), but the measurement was performed in the presence of an additional layer of chicken skin (HAP in tissue/skin, COM in tissue/skin). The acquisition time was 100 s for each spectrum. The spectra are offset for clarity.

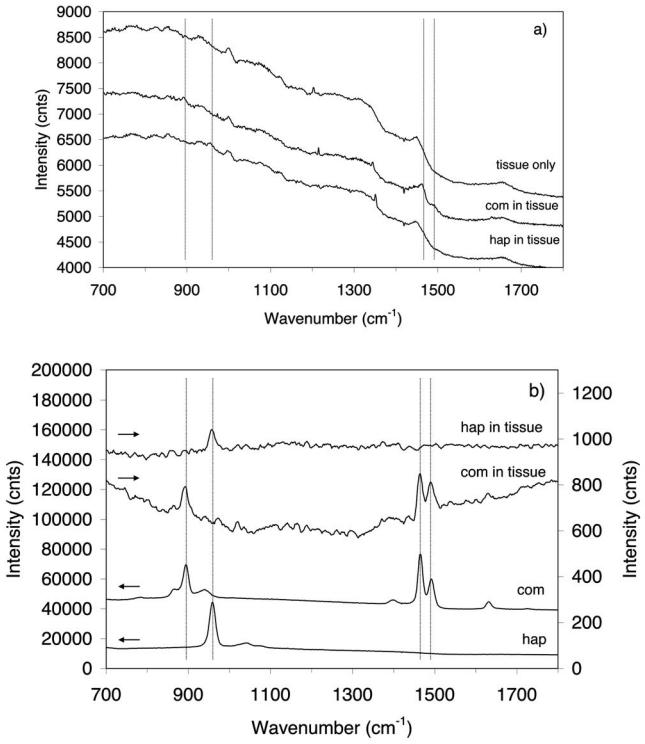

Fig. 5 (a) Raman spectra of calcified material contained within a 100- to 300-μm-thick powder layer smeared in the middle of the tissue slab of an overall tissue thickness of 16 mm (HAP in tissue, COM in tissue), along with the spectra of tissue only measured from the same slab in the absence of the powder layer (tissue only). (b) The Raman spectra of calcified materials obtained by subtracting raw Raman spectra of tissue only from those of tissue containing calcified material, along with the pure Raman spectra of individual calcified materials. The acquisition time was 100 s for each spectrum. The spectra are offset for clarity.

terrupted (i.e., 100% area coverage) smeared layer of 100 to 300 μm thickness. Consequently, by 2 orders, a higher signal-to-noise ratio Raman spectra would be required to detect such a clinically relevant typical calcification cluster and identify its chemical composition. As we show next, this is within the potential of this concept if further technique advances, detailed next, are implemented.

In terms of illumination conditions used, the laser intensity used in our experiments was very low with no potential for sample damage. In fact, the intensity used was only slightly above the maximum permissible exposure, as defined by the stringent laser safety standard BS EN 60825-14:2004 for continuous-wave laser skin illumination at 827 nm, although in this application the potential medical benefits would likely permit exceeding these limits in clinical applications. The code states that up to 34-mW continuous laser power can be deposited within the "limiting aperture" of 3.5 mm diam at 827 nm. This corresponds to around 3.5 mW/mm^2, and our intensity was 4.8 mW/mm^2. This highlights another major advantage of the transmission geometry, its compatibility with defocused beams, promising relatively safe interrogation of deep layers of tissue. Our levels compare well also with the laser illumination intensities used in some other studies *in vivo* at the same wavelength, such as those in work by Enejder et al.,[40] where illumination intensity of 300 mW/mm^2 was used safely. Clearly there is a potential for further increase of this parameter in our experiments, permitting thus still higher signal-to-noise Raman spectra to be obtained.

Additional improvement can be achieved by further optimizing the collection system to collect Raman signals effectively from larger areas. This can be achieved using wider

spectrograph slits, enabling the coupling of a larger number of fibers into the detection system while maintaining the spectral resolution. This can be accomplished, for example, by using larger dispersion gratings in the spectrograph and using a consequently narrower spectral region centered only on the spectral region of interest, for example, on the area where major differences between different calcifications are present and, or in conjunction with, recently developed coded aperture spectroscopy,[41] permitting operations with wider spectrograph slits while maintaining the original spectral resolution.

In quantitative terms, there is a potential to increase the laser power by a factor of 100 to 1000 and operating with further defocused beams and at higher intensities than those used in this study, but still below the damage threshold. Suitable frequency-stabilized diode lasers with internal Bragg gratings capable of reaching the required powers are just emerging on the market. Further improvements can be accomplished by increasing the Raman collection system efficiency by a factor of 10 using the previously mentioned coded aperture concept. Both measures should yield a square root increase in signal-to-noise ratio of the Raman spectra, i.e., approximately 30 to 100 times, permitting a proportional enhancement of sensitivity and enabling the reaching of the required clinically relevant sensitivity for the detection of typical calcification clusters *in vivo*. This large technological advancement obviously needs further experimental validations and this will be the focus of our future studies.

5 Conclusions

We demonstrate the ability of detecting and identifying the chemical composition of calcified material within a clinically relevant depth of 16-mm-thick chicken tissue using transmission Raman spectroscopy. This is the highest depth reported so far (almost doubling previously reported results achieved using SORS[36]) and demonstrates the potential of the concept for reaching, with further improvements, the clinically relevant range for potential application in diagnosis of human breast cancer *in vivo*. Such techniques could be ultimately used in conjunction with the existing mammography or ultrasound techniques to enhance their diagnostic potential.

Acknowledgments

We wish to thank Darren Andrews, Anthony Parker, and Mike Dunne of CCLRC for their support of this work, and the financial contribution of the CLIK Knowledge Transfer, NESTA, and Rainbow Seed Fund enabling this study. Keith Rogers and Rebecca Baker of Cranfield University have strongly supported this study as part of the ongoing program investigating the effect of breast calcifications on the carcinogenesis processes and their potential to enhance understanding and diagnosis.

References

1. Y. Sun, X. R. Zeng, L. Wenger, and H. S. Cheung, "Basic calcium phosphate crystals stimulate the endocytotic activity of cells-inhibition by anti-calcification agents," *Biochem. Biophys. Res. Commun.* **312**, 1053–1059 (2003).
2. A. S. Haka, K. E. Shafer-Peltier, M. Fitzmaurice, J. Crowe, R. R. Dasari, and M. S. Feld, "Diagnosing breast cancer by using Raman spectroscopy," *Proc. Natl. Acad. Sci. U.S.A.* **102**, 12371–12376 (2005).
3. A. S. Haka, K. E. Shafer-Peltier, M. Fitzmaurice, J. Crowe, R. R. Dasari, and M. S. Feld, "Identifying differences in microcalcifications in benign and malignant breast lesions by probing differences in their chemical composition using Raman spectroscopy," *Cancer Res.* **62**, 5375–5380 (2002).
4. R. E. Lenkinski, M. Ahmed, A. Zaheer, J. V. Frangioni, and S. N. Goldberg, "Near-infrared imaging of microcalcifications in the animal model of breast cancer," *Acad. Radiol.* **10**, 1159–1164 (2003).
5. S. F. Weng, X. F. Ling, and Y. Y. Song, "FTIR fiber optics and FT-Raman spectroscopic studies for the diagnosis of cancer," *Am. Clin. Lab.* **19**, 20 (2000).
6. R. K. Dukor, M. N. Liebman, and B. L. Johnson, "A new, nondestructive method for analysis of clinical samples with FT-IR microspectroscopy. Breast cancer tissue as an example," *Cell Mol. Biol. (Paris)* **44**, 211–217 (1998).
7. T. C. Bakker Schut, M. J. H. Witjes, H. J. C. M. Sterenborg, O. C Speelman, J. L. N. Roodenburg, E. T. Marple, H. A. Bruining, and G. J. Puppels, "*In vivo* detection of dysplastic tissue by Raman spectroscopy," *Anal. Chem.* **72**, 6010–6018 (2000).
8. A. Mahadevan-Jansen and R. R. Richards-Kortum, "Raman spectroscopy for the detection of cancers and precancers," *J. Biomed. Opt.* **1**, 31–70 (1996).
9. N. Stone, C. Kendall, N. Shepherd, P. Crow, and H. Barr, "Near-infrared Raman spectroscopy for the classification of epithelial pre-cancers and cancers," *J. Raman Spectrosc.* **33**, 564–573 (2002).
10. N. Stone, C. Kendall, J. Smith, P. Crow, and H. Barr, "Raman spectroscopy for identification of epithelial cancers," *Faraday Discuss.* **126**, 141–157 (2003).
11. S. Rehman, P. A. Revell, and I. Rehman, "Analysis of breast cancer tissues by Fourier transform infrared rapid scan imaging," *J. Clin. Oncol.* **23**, 216S–216S (2005).
12. P. Matousek and A. W. Parker, "Bulk Raman analysis of pharmaceutical tablets," *Appl. Spectrosc.* **60**, 1353–1357 (2006).
13. M. L. Myrick, S. M. Angel, and R. Desiderio, "Comparison of some fiber optic configurations for measurement of luminescence and Raman-scattering," *Appl. Opt.* **29**, 1333–1344 (1990).
14. J. Wu, Y. Wang, L. Perelman, I. Itzkan, R. Dasari, and M. S. Feld, "3-dimensional imaging of objects embedded in turbid media with fluorescence and Raman-spectroscopy," *Appl. Opt.* **34**, 3425–3430 (1995).
15. C. J. H. Brenan and I. W. Hunter, "Volumetric Raman microscopy through a turbid medium," *J. Raman Spectrosc.* **27**, 561–570 (1996).
16. B. B. Das, F. Liu, and R. R. Alfano, "Time-resolved fluorescence and photon migration studies in biomedical and model random media," *Rep. Prog. Phys.* **60**, 227–292 (1997).
17. H. Koizumi, Y. Yamashita, A. Maki, T. Yamamoto, Y. Ito, H. Itagaki, and R. Kennan, "Higher-order brain function analysis by trans-cranial dynamic near-infrared spectroscopy imaging," *J. Biomed. Opt.* **4**, 403–413 (1999).
18. J. C. Hebden, A. Gibson, R. Yusof, N. Everdell, E. M. C. Hillman, D. T. Delpy, S. R. Arridge, T. Austin, J. H. Meek, and J. S. Wyatt, "Three-dimensional optical tomography of the premature infant brain," *Phys. Med. Biol.* **47**, 4155–4166 (2002).
19. N. Everall, T. Hahn, P. Matousek, A. W. Parker, and M. Towrie, "Picosecond time-resolved Raman spectroscopy of solids: capabilities and limitations for fluorescence rejection and the influence of diffuse reflectance," *Appl. Spectrosc.* **55**, 1701–1708 (2001).
20. P. Matousek, M. Towrie, A. Stanley, and A. W. Parker, "Efficient rejection of fluorescence from Raman spectra using picosecond Kerr gating," *Appl. Spectrosc.* **53**, 1485–1489 (1999).
21. P. Matousek, M. Towrie, C. Ma, W. M. Kwok, D. Phillips, W. T. Toner, and A. W. Parker, "Fluorescence suppression in resonance Raman spectroscopy using a high-performance picosecond Kerr gate," *J. Raman Spectrosc.* **32**, 983–988 (2001).
22. M. D. Morris, P. Matousek, M. Towrie, A. W. Parker, A. E. Goodship, and E. R. C. Draper, "Kerr-gated time-resolved Raman spectroscopy of equine cortical bone tissue," *J. Biomed. Opt.* **10**, 014014 (2005).
23. E. R. C. Draper, M. D. Morris, N. P. Camacho, P. Matousek, M. Towrie, A. W. Parker, and A. E. Goodship, "Novel assessment of bone using time-resolved transcutaneous Raman spectroscopy," *J. Bone Miner. Res.* **20**, 1968–1972 (2005).
24. P. Matousek, N. Everall, M. Towrie, and A. W. Parker, "Depth profiling in diffusely scattering media using Raman spectroscopy and picosecond Kerr gating," *Appl. Spectrosc.* **59**, 200–205 (2005).

25. N. Everall, T. Hahn, P. Matousek, A. W. Parker, and M. Towrie, "Photon migration in Raman spectroscopy," *Appl. Spectrosc.* **58**, 591–597 (2004).
26. P. Matousek, I. P. Clark, E. R. C. Draper, M. D. Morris, A. E. Goodship, N. Everall, M. Towrie, W. F. Finney, and A. W. Parker, "Subsurface probing in diffusely scattering media using spatially offset Raman spectroscopy," *Appl. Spectrosc.* **59**, 393–400 (2005).
27. P. Matousek, M. D. Morris, N. Everall, I. P. Clark, M. Towrie, E. Draper, A. Goodship, and A. W. Parker, "Numerical simulations of subsurface probing in diffusely scattering media using spatially offset Raman spectroscopy," *Appl. Spectrosc.* **59**, 1485–1492 (2005).
28. M. V. Schulmerich, W. F. Finney, R. A. Fredricks, and M. D. Morris, "Subsurface Raman spectroscopy and mapping using a globally illuminated non-confocal fiber-optic array probe in the presence of Raman photon migration," *Appl. Spectrosc.* **60**, 109–114 (2006).
29. P. Matousek, E. R. C. Draper, A. E. Goodship, I. P. Clark, K. L. Ronayne, and A. W. Parker, "Noninvasive Raman spectroscopy of human tissue *in vivo*," *Appl. Spectrosc.* **60**, 758–763 (2006).
30. M. V. Schulmerich, W. F. Finney, V. Popescu, M. D. Morris, T. M. Vanasse, and S. A. Goldstein, "Transcutaneous Raman spectroscopy of bone tissue using a non-confocal fiber optic array probe," *Proc. SPIE* **6093**, 60930O (2006).
31. P. Matousek, "Inverse spatially offset Raman spectroscopy for deep non-invasive probing of turbid media," *Appl. Spectrosc.* **60**, 1341–1347 (2006).
32. M. V. Schulmerich, K. A. Dooley, M. D. Morris, T. M. Vanasse, and S. A. Goldstein, "Transcutaneous fiber optic Raman spectroscopy of bone using annular illumination and a circular array of collection fibers. Indicators of bone quality," *J. Biomed. Opt.* **11**(6), 060502 (2006).
33. P. Matousek and A. W. Parker, "Non-invasive Raman Spectroscopy of Pharmaceutical Capsules," *J. Raman Spectrosc.* (to be published).
34. Cancer Research UK web pages, http://www.cancerhelp.org.uk/help/default.asp?page=5075.
35. R. Baker, P. Matousek, K. Ronayne, A. W. Parker, K. Rogers, and N. Stone, "Depth profiling of calcifications in breast tissue using picosecond Kerr-gated Raman spectroscopy," *Analyst (Cambridge, U.K.)* **132**, 48–53 (2007).
36. N. Stone, R. Baker, K. Rogers, A. W. Parker, and P. Matousek, "Future possibilities in the diagnosis of breast cancer by subsurface probing of calcifications with surface offset Raman spectroscopy (SORS)," Analyst (Cambridge, U.K.) (submitted for publication).
37. G. Mitic, J. Kolzer, J. Otto, E. Plies, G. Solkner, and W. Zinth, "Time-gated transillumination of biological tissuelike phantoms," *Appl. Opt.* **33**, 6699–6710 (1994).
38. F. Sardanelli, F. Zandrino, A. Imperiale, E. Bonaldo, M. G. Quartini, and N. Cogorno, "Breast biphasic compression versus standard monophasic compression in x-ray mammography," *Radiology* **217**, 576–580 (2000).
39. S. L. Olson, B. W. Fam, P. F. Winter, F. J. Scholz, A. K. Lee, and S. E. Gordon, "Breast calcifications: Analysis of imaging properties," *Radiology* **169**, 329–332 (1988).
40. A. M. K. Enejder, T. G. Scecina, J. Oh, M. Hunter, W. C. Shih, S. Sasic, G. L. Horowitz, and M. S. Feld, "Raman spectroscopy for noninvasive glucose measurements," *J. Biomed. Opt.* **10**, 031114 (2005).
41. S. T. McCain, M. E. Gehm, Y. Wang, N. P. Pitsianis, and D. J. Brady, "Coded aperture Raman spectroscopy for quantitative measurements of ethanol in a tissue phantom," *Appl. Spectrosc.* **60**, 663–671 (2006).